COMMUNICATION

Controlled Synthesis of Organic/Inorganic van der Waals Solid for Tunable Light–Matter Interactions

Lin Niu, Xinfeng Liu, Chunxiao Cong, Chunyang Wu, Di Wu, Tay Rong Chang, Hong Wang, Qingsheng Zeng, Jiadong Zhou, Xingli Wang, Wei Fu, Peng Yu, Qundong Fu, Sina Najmaei, Zhuhua Zhang, Boris I. Yakobson, Beng Kang Tay, Wu Zhou, Horng Tay Jeng, Hsin Lin, Tze Chien Sum, Chuanhong Jin, Haiyong He,* Ting Yu,* and Zheng Liu*

Van der Waals (vdW) solids are vertically stacked heterostructures that consist of different layered components. These materials have opened a window into a new landscape of next generation electronics and optoelectronics such as transistors,[1–5] sensors,[6–8] photodetectors,[9–14] and spin-valleytronic devices.[15–17] In light of the discoveries in inorganic 2D crystals, such as graphene,[5,7,18] hexagonal boron nitride (h-BN),[5,19,20] and transition metal dichalcogenides (TMDs),[21,22] one could engineer composition, thickness, and stacking sequences of layered components in vdW solids for design of new material architectures and properties suited for specific applications.

Light–matter interaction at the interfaces of vdW solids is the key to build high-performance optoelectronic devices. Such interfaces have been realized in inorganic WS$_2$/graphene vdW solids.[10] In order to engineer an excellent inorganic/organic interface for the study of light–matter interaction, a suitable photoactive material needs to be identified. Recently, among plenteous photoactive materials, inorganic–organic perovskites have attracted great attention due to their remarkable performance and relatively low cost as good lighter absorbers in solid-state photovoltaic devices.[23–26] Perovskites have shown highly stable excitons,[27] strong exciton absorption, sharp exciton emission even at room temperature,[28,29] high optical absorption coefficient, optimal band gap, and long electron/hole diffusion lengths,[23] which grant their high efficiencies for energy conversion. The highest efficiency of organometal perovskite is ≈20%.[30] It turns out that the performance of the inorganic–organic perovskite devices highly relies on the material quality and the surfaces. Various 2D layers could be excellent substrates for such materials and one should examine their interfacial impact, in greater details, on the optical properties of perovskite.[26] These expected complementary properties of such hybridizations suggest that marrying inorganic 2D materials with inorganic–organic perovskites may provide opportunities to understand the light–matter interactions at their hetero-interfaces. Although this organic perovskite/2D heterostructure has shown promising light-based potentials in the visible regime, the difficulty of fabrication remains.

Dr. L. Niu, Dr. H. Wang, Dr. Q. Zeng, J. Zhou, Dr. W. Fu,
Dr. P. Yu, Q. Fu, Dr. H. He, Prof. Z. Liu
School of Materials Science and Engineering
Nanyang Technological University
Singapore, Singapore 639798, Singapore
E-mail: HYHe@ntu.edu.sg; Z.Liu@ntu.edu.sg
Dr. X. Liu, Dr. C. Cong, Prof. T. C. Sum, Prof. T. Yu
School of Physical and Mathematical Sciences
Nanyang Technological University
Singapore, Singapore 637371, Singapore
E-mail: YuTing@ntu.edu.sg
Dr. X. Liu
National Center for Nanoscience and Technology
Beijing 100190, China
Dr. C. Wu, Prof. C. Jin
State Key Laboratory of Silicon Materials and
School of Materials Science and Engineering
Zhejiang University
Hangzhou 310027, P. R. China
D. Wu, Prof. H. Lin
Centre for Advanced 2D Materials and Department of Physics
National University of Singapore
Singapore, Singapore 117542, Singapore

T. R. Chang, Prof. H. T. Jeng
Department of Physics
National Tsing Hua University
Hsinchu 30013, Taiwan
X. Wang, Prof. B. K. Tay, Prof. Z. Liu
NOVITAS
Nanoelectronics Centre of Excellence
School of Electrical and Electronic Engineering
Nanyang Technological University
Singapore 639798, Singapore
Dr. S. Najmaei
United States Army Research Laboratories
Sensors and Electron Devices Directorate
2800 Powder Mill Road, Adelphi
MD 20783, USA
Dr. Z. Zhang, Prof. B. I. Yakobson
Department of Materials Science and Nanoengineering
Rice University
Houston, TX 77005, USA
Dr. W. Zhou
Materials Science and Technology Division
Oak Ridge National Lab
Oak Ridge, TN 37831, USA

To date, most inorganic vdW solids such as graphene/h-BN, graphene/MoS$_2$, MoS$_2$/WS$_2$, graphene/h-BN superlattice, and graphene/h-BN/MoS$_2$ stacks were engineered via layer-by-layer transfer of 2D films. By using the similar method, inorganic–organic perovskite films will suffer from the organic solutions used during the transfer process.[7,19,31–34] Moreover, it generally requires a few cycles of dry transfer, alignment, e-beam lithography, plasma etching, and metal deposition to engineer vdW devices,[1] which may have detrimental effects on perovskite quality. Recently, deposition technologies such as chemical vapor deposition (CVD) have been applied to prepare vdW solids such as BN/graphene and TMD vdW heterostructures.[2,35–39] In order to address these problems, we propose a three-step method for controlled synthesis of organic/inorganic vdW solids. This protocol enables production of large-size and highly crystalline inorganic/organic vdW solid families. The inorganic monolayers could be substituted by many available 2D materials. Surprisingly, in such organic/inorganic interfaces, the subnanometer monolayer beneath the organic component can dramatically tune the optical properties of the vdW solids, by coupling with the electron-hole generated in the organic perovskites. Further studies reveal that h-BN monolayer is an excellent complement to organic perovskites for preserving their original optical properties, as also supported by theoretical calculation and the patterned organic perovskite/h-BN vdW solids as red light emitters. This work

shines light on ways for designing vdW solids with great potential for a wide variety of applications in optoelectronics.

The feasibility of the strategy and method developed have been demonstrated by using the most popular carbon-based 2D material, graphene, and noncarbon 2D materials, h-BN and MoS$_2$, as the substrates for growing the organic/inorganic vdW solids. First, large-size 2D monolayers are prepared as inorganic components (Figures S1–S4, Supporting Information). Next, epitaxial growth of highly crystalline PbI$_2$ nanoplatelets on the prefabricated 2D substrates is performed via a physical vapor deposition (PVD) process. The PbI$_2$ crystals are then converted into perovskite by reacting with CH$_3$NH$_3$I under vacuum, forming organic perovskite (methylammonium lead halide)/2D vdW solids, denoted as perovskite/2D vdW solids. The morphologies of the organic perovskite/2D vdW solids were examined by optical microscopy, scanning electron microcopy (SEM), and atomic force microscopy (AFM) (see **Figure 1** and Figures S5–S7 in the Supporting Information). The CH$_3$NH$_3$PbI$_3$ nanoplatelets display different colors in the optical images, responding to different thickness. Their surface roughness is measured to be ≈2.0 nm by AFM in Figures S6–S7 (Supporting Information), indicating the high quality of the perovskite/2D vdW solids. Organic perovskites sitting on polycrystalline graphene, h-BN films and single crystal MoS$_2$ domains are illustrated in Figure 1g–i, respectively. The yellow, gray, and blue balls correspond to organic molecule
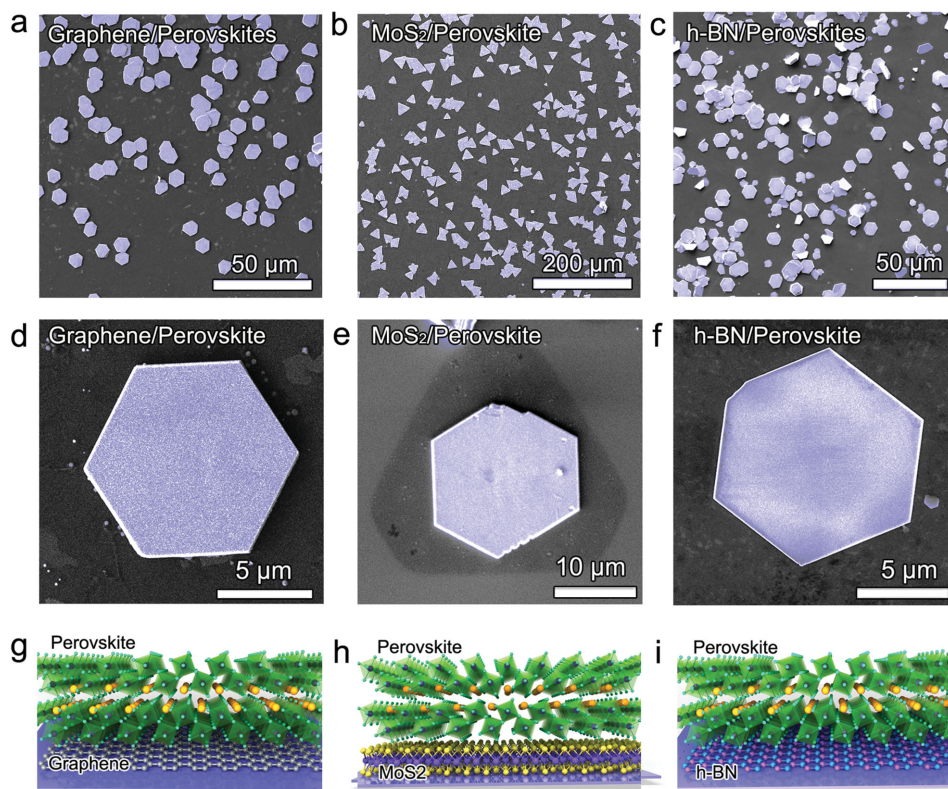
Figure 1. Overall morphologies of the perovskite/2D vdW solids. a–f) False-colored SEM images of perovskite 2D vdW solids on a,d) graphene, b,e) MoS$_2$, and c,f) h-BN, respectively. Their corresponding structure models are illustrated in panels (g, h, and i), respectively. a,d) Graphene and c,f) h-BN films cover the whole SiO$_2$/Si substrates while b,e) triangular MoS$_2$ single-crystal domains are directly grown on SiO$_2$/Si substrates. a–f) Hexagonal and triangular organic perovskites are all in light blue. In the structure models (g–i), the yellow, gray, and blue balls are organic molecule CH$_3$NH$_3$$^+$ ions, Pb atoms, and I atoms, respectively. Pb atoms locate at the center of the halide octahedrons.
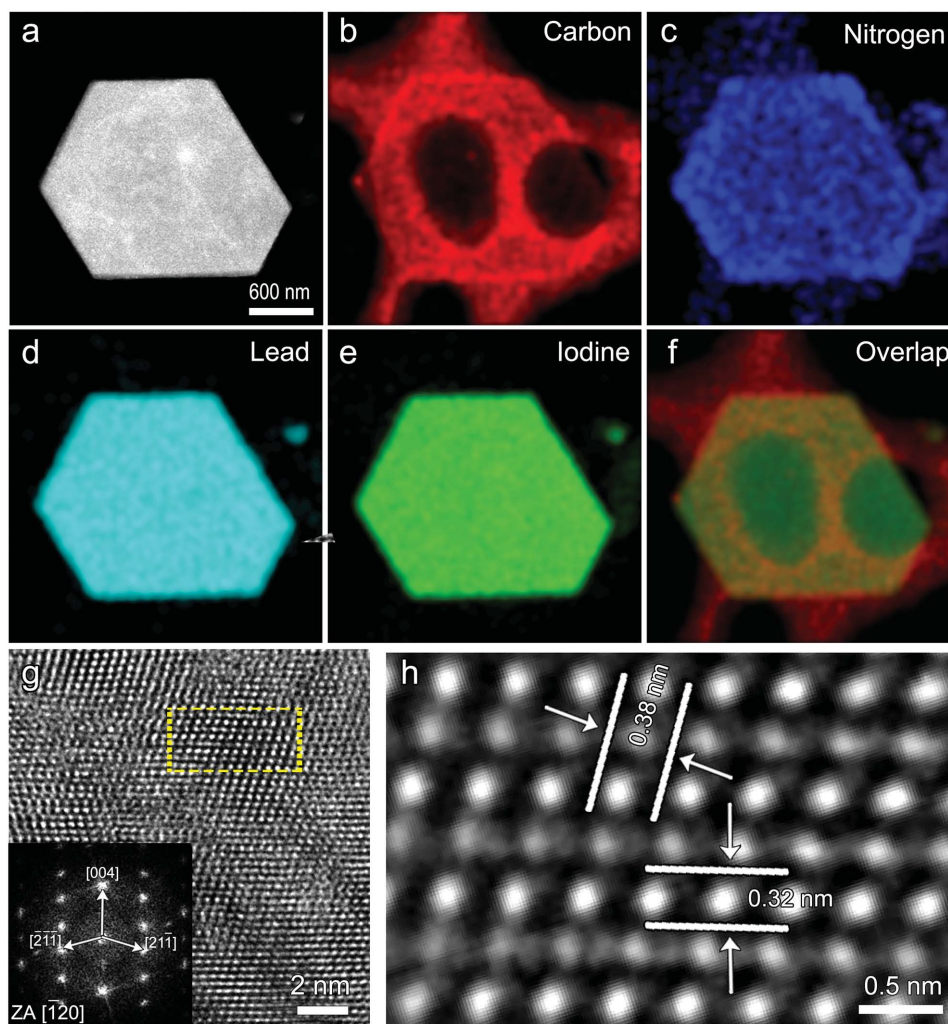
Figure 2. Electron microscopy characterization of the perovskite/2D vdW solids. a) Low-resolution STEM image of a perovskite platelet. b–f) Element mapping obtained by energy-dispersive X-ray spectroscopy show the uniformity of the perovskite nanoplatelets. g) High resolution TEM (HRTEM) image showing the structure of the perovskite nanoplatelets. Inset is the corresponding fast Fourier transform pattern from this HRTEM image along the [−120] zone axis (ZA). h) Filtered HRTEM image of the area highlighted in (g).

$CH_3NH_3^+$ ions, Pb atoms, and I atoms, respectively. In the octahedral structure of the PbI_2, Pb atoms locate at the center of the halide octahedrons. During the conversion, CH_3NH_3I reacts with PbI_2, and the $CH_3NH_3^+$ ions (orange balls in the schematic) insert into the octahedral structure of PbI_2 and stay at the center of eight lead halide octahedrons. XRD patterns of perovskite nanoplatelets are examined to evaluate the quality of perovskite/2D vdW solids. For converted perovskite vdW solids, peaks at 14.06°, 28.38°, 3l.74°, and 43.14° are located, assigned to (110), (220), (310), and (330), respectively, for $CH_3NH_3PbI_3$ perovskite with a tetragonal crystal structure (Figures S8–S10, Supporting Information).[40] It is worth noting that all the 2D monolayers we used in our experiments remain intact during the conversion.

The quality of as-grown organic perovskites has been further examined by selected area electron diffraction (SAED), high-resolution transmission electron microscopy (HRTEM) imaging, and energy dispersive X-ray spectroscopy (EDX)

(**Figure 2**; Figures S11–S13, Supporting Information). HRTEM imaging indicates a highly crystalline PbI_2 with sixfold symmetric diffraction patterns from selected area electron diffraction (details of the TEM results of PbI_2 nanoplatelets can be found in Figures S11 and S12 in the Supporting Information). Then, we investigate the crystal structure transformations with a complete conversion process from PbI_2 into $CH_3NH_3PbI_3$. Figure 2a shows a typical perovskite flake and the corresponding elemental mapping of carbon (C), nitrogen (N), lead (Pb), and iodine (I) are presented in Figure 2b–e, followed by an overlapped image in Figure 2f. This mapping confirms the elemental uniformity of the perovskite over the whole flake after conversion. In addition to XRD spectra, the crystal structure of the converted perovskite is evaluated by HRTEM imaging in Figure 2g,h. The lattice of perovskite is quite clear in Figure 2g. Inset is the corresponding fast Fourier transform (FFT) pattern from this HRTEM image along the [−120] zone axis (ZA). During the conversion process from PbI_2 into perovskite, with
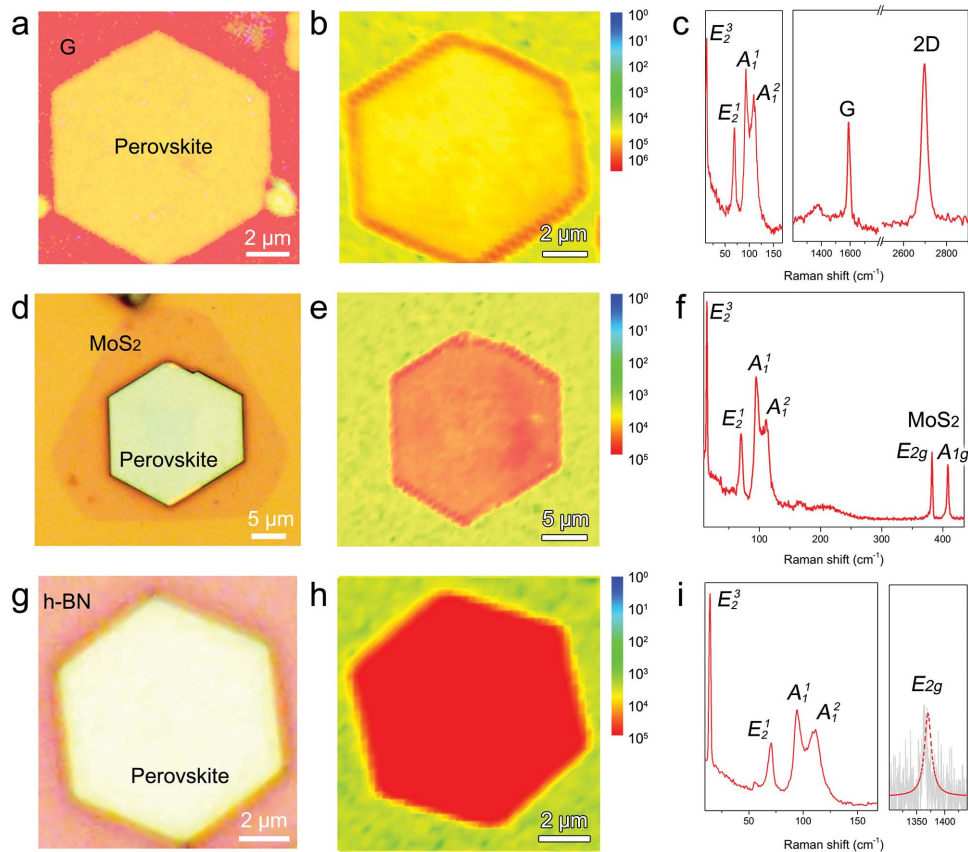
Figure 3. Raman characterization of the perovskite/2D vdW solids. a,d,g) Optical images of perovskite grown on graphene, MoS_2 and h-BN, respectively. Scale bars are 2, 5, and 2 µm, respectively. b,e,h) Corresponding Raman intensity mapping of phonon modes of A_1^1 and A_1^2 of the perovskite/2D vdW solids. c,f,i) Corresponding Raman spectra of the perovskite/2D vdW solids. The presence of graphene, MoS_2 and h-BN layers underneath the perovskite can be confirmed by the peaks at 1590 cm^{-1} (G mode of graphene), 382 and 408 cm^{-1} (E_{2g} and A_{1g} modes of MoS_2), and 1369 cm^{-1} (E_{2g} mode of h-BN), respectively. The excitation wavelength used for Raman measurements is 532 nm.

the chemical reaction of CH_3NH_3I and PbI_2, the space group is transferred from $P3m1$ for $PbI2$ into $I4cm$ for perovskite. Figure 2h shows a close-up of the area from the yellow dashed rectangle in Figure 2g. The interplanar distances of ≈0.38 and ≈0.32 nm can be determined, which are attributed to the (21–1) planes and (004) planes, respectively, with the tetragonal lattice of perovskite. The corresponding structural schematic of the perovskite are be found in Figure S13c (Supporting Information). Apparently, along the [001] direction, there are alternative lines, similar to the HRTEM results in Figure 2g. One consists of I and Pb atoms, while another consists of I atoms and $CH_3NH_3^+$ ions.

Confocal micro-Raman mapping and spectroscopy are commonly used powerful tools to characterize materials thanks to their unique advantages of relatively high spatial resolution (a few hundreds of nanometer), no requirement for special sample preparation, high efficiency, and non-destructiveness. **Figure 3** shows the micro-Raman mapping and spectroscopy of the perovskite/2D vdW solids. Optical images of hexagonal perovskite nanoplatelets sitting on CVD graphene, MoS_2, and h-BN are shown in Figure 3a,d,g. The thickness of the perovskite nanoplatelets on CVD graphene, MoS_2, and h-BN are around 300, 290, and 270 nm, respectively (see Figure S9 in

the Supporting Information). Figure 3b,c, e,f, and h,i are the corresponding Raman mapping and spectra of the perovskite/graphene, perovskite/MoS_2, and perovskite/h-BN, respectively. It can be seen from the Raman images of the sum intensity of A_1^1 and A_1^2 modes that the perovskite nanoplatelets grown on CVD graphene, MoS_2, and h-BN are homogenous. In the measured spectroscopy range of 10–160 cm^{-1}, the Raman spectra reveal four distinct bands at ≈14, 70, 94, and 110 cm^{-1} as shown in Figure 3c,f,i, which indicate that the perovskite nanoplatelets maintain the 4H polytype of PbI_2 (see Figure S14 in the Supporting Information).[41] The phonon vibration located at ≈14 cm^{-1} was assigned to E_2^3, the shear-motion rigid-layer mode of PbI_2 with 4H polytype,[41] while the Raman peaks at ≈70, 94, and 110 cm^{-1} were assigned to E_2^1, A_1^1, and A_1^2, respectively.[42] The presence of graphene, MoS_2, and h-BN layers underneath the perovskite are confirmed by the Raman peaks at 1590 cm^{-1} (G mode of graphene), 382 and 408 cm^{-1} (E_{2g} and A_{1g} modes of MoS_2), and 1369 cm^{-1} (E_{2g} mode of h-BN) as shown in Figure 3c,f,i, respectively.

We also explore the UV–vis absorption and PL excitation spectra of the perovskite/2D vdW solids on quartz. The absorption peak (760 nm) of perovskite/2D vdW solids is attributed to the direct gap transition from the valence band maximum to

COMMUNICATION
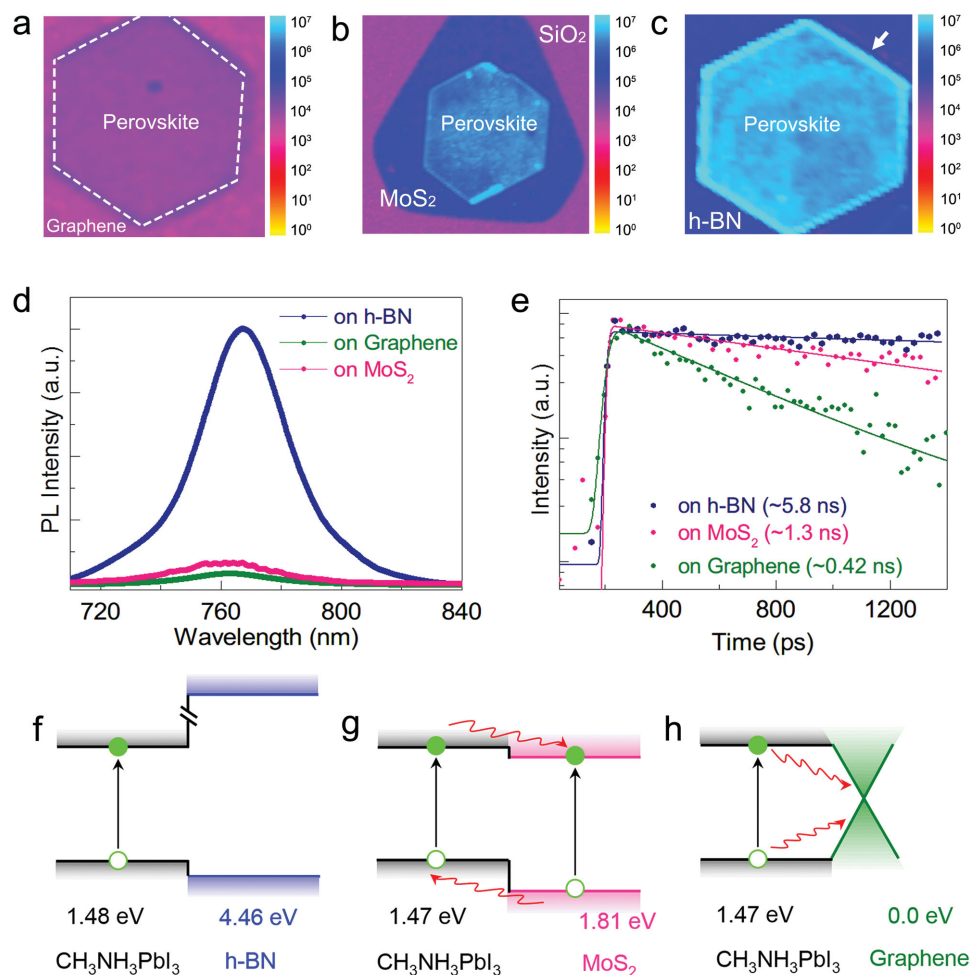
Figure 4. Photoluminescence of the perovskite/2D vdW solids. a–c) PL intensity mapping of perovskite on graphene, MoS$_2$ and h-BN, respectively. The mapping is collected at 760 nm under the same conditions. Considerable difference in the PL intensity of the perovskites is found on graphene (purple in (a), ≈10^4), MoS$_2$ (blue in (b), ≈10^6), and h-BN (light blue in (c), ≈10^7), respectively. The profile of the MoS$_2$ layer is also found in dark blue in (b). d) Comparison of the PL spectra extracted from the PL mapping. e) Time-resolved PL decay transients measured at 760 ± 10 nm for perovskites on h-BN (light blue, lifetime of 5.8 ± 0.5 ns), MoS$_2$ (blue, lifetime of 1.3 ± 0.25 ns), and graphene (purple, lifetime of 0.42 ± 0.01 ns). The excitation wavelength for PL measurements is 532 nm. The solid lines in (e) are the single-exponential fits of the PL decay transients. f–h) Schematic band alignment and illustrative transfer of photo-excited carriers at the f) perovskite/*h*-BN, g) perovskite/MoS$_2$, and h) perovskite/graphene hetero-interfaces.

the conduction band minimum (Figure S15, Supporting Information). It is found that all the absorption peaks are similar to those previously reported, where PbI$_2$ and perovskites are prepared by spinning coating and vapor deposition. These results indicate that the 2D monolayers do not change the excitation absorption of organic perovskites.[23,25] In order to examine the importance of the hetero-interface in perovskite/2D vdW solids, we characterize the samples using photoluminescence (PL) spectroscopic techniques, including PL spectrum, PL mapping, and time-resolved PL measurement, as presented in **Figure 4**. Figure 4a–c shows the PL mapping of perovskite (mapping wavelength at ≈760 nm) on graphene, MoS$_2$, and h-BN, respectively. All the maps are collected under the same conditions. Their optical images are shown in Figure 3a,d,g, respectively. For comparison, the three PL mapping images are displayed using the same scale bar with the PL intensity ranging from 1 to 10^7. It turns out that the PL emission in per-

ovskite is significantly modulated by the inorganic 2D components. For perovskite/graphene vdW solid, little contrast can be found. The PL emission is completely quenched (only a little intensity difference between perovskite and graphene). However, for perovskite/MoS$_2$, a sharp contrast can be observed from SiO$_2$ substrate (purple), monolayer MoS$_2$ (dark blue), and perovskite/MoS$_2$ (blue). In perovskite/h-BN, a much higher PL intensity from perovskite is recorded. The intensity is ≈10^3 stronger than that on perovskite/graphene vdW solids. Their representative PL spectra are shown in Figure 4d. In addition, the PL intensity mapping in Figure 4c also shows distinctly different from the edge to the core region, as indicated by the white arrow, and the shape of outer layer has a consistent morphology layout as that observed in the optical microscopy image. It is ascribed to light scattering effect at edges that caused the difference of emission intensity at side and core regions. In order to understand the carrier dynamics at these

distinct hetero-interfaces, time-resolved PL measurements are conducted as shown in Figure 4e. From the single decay fitting, the lifetimes for perovskite/h-BN (green), perovskite/MoS$_2$ (pink), and perovskite/graphene (navy) vdW solids are 5.8, 1.3, and 0.42 ns, respectively. The lifetime of the perovskite/h-BN is comparable to previous reported value of ≈6.8 ns for perovskite on mica, suggesting almost no charge transfer at the interface,[43] and thus the combining rate of the electron-hole pairs remains intact on h-BN due to the very large optical band gap of h-BN (≈6.0 eV). It is a fascinating venue to preserve the intrinsic optical properties of perovskite by using this uniform, smooth, and nonconductive h-BN monolayer (see Figure 4f). In contrast, the exciton lifetime in the perovskite/MoS$_2$ interface drops remarkably, indicating that considerable charge transfer occurs at the interface. Our calculations estimate that such interface has a type II band alignment with band offset of ≈0.3 eV (Figure 4g), which provides a strong driving force to separate the electron-hole pairs excited by photons. Moreover, as the electron-hole pairs in the perovskite have a small binding energy,[44] they are particularly easy to split under a built-in electric field across the interface. Such effect dominates the carrier dynamics at perovskite/graphene interface, as evidenced by the entirely quenching behavior. In this situation, graphene has linear band dispersion with a zero band gap, which renders graphene as a collector for both electrons[45] and holes[46] transferred from the perovskite (Figure 4h). As such, carriers can hardly survive in the perovskites and thereby no PL peak can be measured. This efficient process for charge transfer has been demonstrated and served as electron collection layer and high performance hybrid photodetectors.[45] Therefore, tailoring the interfaces provides us an efficient way to tune and design the light–matter interactions in 2D material based heterostructures, which will benefit the fabrication of layered material based optoelectronic devices such as photodetectors, photovoltaics, light emission diodes, and on-chip lasers.

Understanding the growing mechanism is the key to improving the quality of perovskite/2D vdW solids and engineering the organic/inorganic interfaces. Ex situ time dependent experiments are carried out to clarify this. The samples with different reaction time (t_R) are synthesized and characterized by optical microscopy to monitor the evolution of PbI$_2$ nanoplatelets. As shown in Figure S21 (Supporting Information), only small red dots can be observed at the early stage of the reaction ($t_R = 1$ min). Our density functional theory (DFT)-based calculations estimate that the diffusion of a PbI$_2$ nanoflake (2 nm in size) on the h-BN substrates is around 50 meV, thus being highly mobile (Figure S22a, Supporting Information). When the reaction time is increased to 5 min, plenty of PbI$_2$ nanoplatelets with irregular shape were formed and some of these PbI$_2$ nanoplatelets tend to coalesce with each other. The coalescence process is energetically favorable because it reduces the edge energy of PbI$_2$ nanoplatelets by decreasing their total edge length. Moreover, the rotation barrier of the nanoplatelets is also rather small, being only 45 meV for a 2 nm diameter nanoflake on a monolayer h-BN sheet (Figure S22b, Supporting Information). Thus, the nanoplatelets can readily adjust their crystal orientations during the coalescence process so that the misoriented interfaces (or grain boundaries) can be largely avoided. This fact agrees with our TEM characterization

that the PbI$_2$ nanoplatelets can be in a single crystal over tens of micrometer size. Finally, by extending the reaction time to 20 min, the density of nuclei is decreased dramatically and hexagonal PbI$_2$ appears. On the basis of gradual morphology evolution, we propose that PbI$_2$ is formed through a van der Waals epitaxy mechanism. According to the time dependent experiments, there are two key points in the growth of perovskite/2D vdW solids: nucleation site and van der Waals epitaxy. This assumption is further supported by our perovskite/2D vdW patterns (**Figure 5**), where the 2D materials are patterned into arrays to separate nucleation sites (the dangling bonds within the 2D materials) from a defect-free surface. In a brief summary, initially, PbI$_2$ nanoparticles are nucleated around the edges and defects of 2D materials. These nanoparticles then grew along surface of 2D materials and began to merge to form highly crystalline nanoplatelets. Next, the PbI$_2$ nanoplatelets extended on 2D material surface and covered all the area shown in Figure S23a,d,g (Supporting Information). Finally PbI$_2$ will be converted into organic perovskite.

Inspired by the discussion above, based on our expertise on the controlled growth of perovskite/2D vdW and understanding of the charge transfer dynamic at the interfaces, patterned perovskite/h-BN vdW solids have been demonstrated and show excellent light emission performance as shown in Figure 5. Considering that it is energetically favorable for the PbI$_2$ to nucleate at the defects, one could control the growth of PbI$_2$ and perovskite by predesigning the 2D films. First, periodic h-BN patterns are patterned by lithography (Figure S24, Supporting Information). Then PbI$_2$ is deposited on h-BN arrays via PVD methods. Finally, patterned perovskite/h-BN vdW solids are obtained after conversion. It is worth noting that the patterning of 2D films is compatible with traditional lithography processing. Perovskite/2D vdW solids with arbitrary geometries could be fabricated by this approach. Figure 5a presents the SEM image of perovskite/h-BN disk array in a hexagonal densely packed arrangement with patch diameter of $d = 20$ μm and space distance of $D = 50$ μm. All the h-BN patches are covered by perovskites without missing pixel, and the space between patches is very clean, indicating that our method can effectively control the growth of perovskite/2D vdW solid on targeted area. Figure 5c shows the "NTU" array derived from Figure S18b (Supporting Information), where one can see clearly how the "NTU" array of perovskite/2D vdW solid formed. The diameter of the perovskite/h-BN hexagonal patches in the "NTU" array is around 10 μm and the gap distance between all adjacent patches is 10 μm. The gap distance between all adjacent "NTU" units is around 30 μm. Fluorescent microscopy images were taken under the excitation of irradiation (365 nm) from a high pressure mercury lamp (Figure 5b,d). Bright red luminescent patterns can be seen unambiguously without defects. The dark regions in Figure 5b,c correspond to the spaces without perovskite.

In summary, organic perovskite/2D vdW solids are prepared via a three-step process. Such vdW solids can be grown in a scalable fashion and designed into arbitrary shapes by prepatterning the inorganic 2D monolayer using lithography. Highly crystalline organic perovskite crystals are confirmed by geometric, spectroscopic, and chemical analysis. Distinct organic/inorganic interfaces are formed by using various 2D
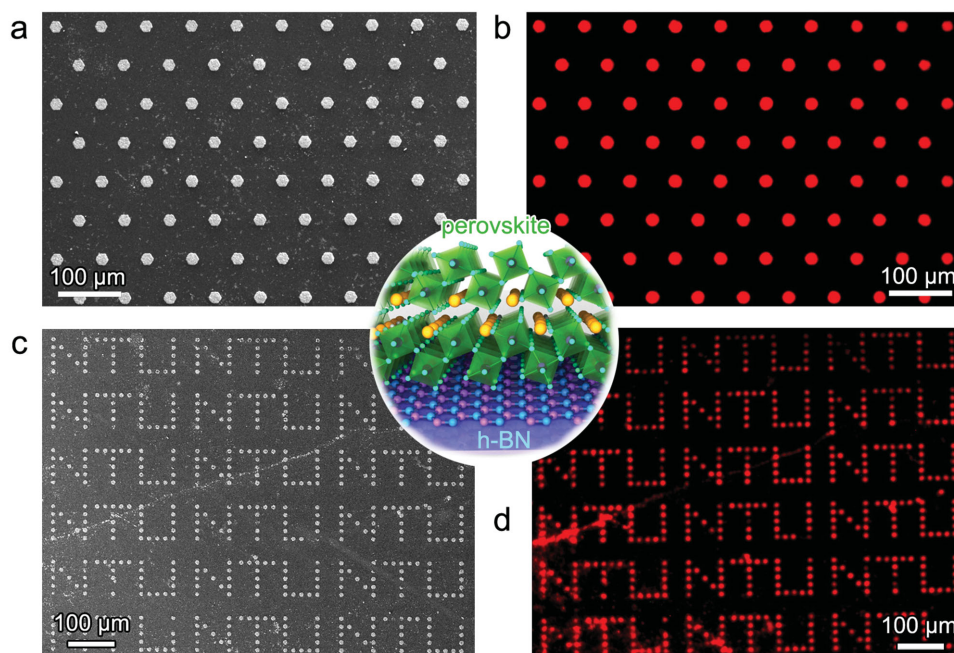
Figure 5. Patterned perovskite/h-BN vdW solids for red light emitting array. a) SEM image of a perovskite/h-BN dotted array. The diameter of the dots is ≈20 µm and the spacing is ≈50 µm. b) Corresponding fluorescent image showing a high intensity emission of red light. c) SEM and d) fluorescent image of perovskite/h-BN "NTU" arrays. The diameter of perovskite/h-BN hexagonal patches in the NTU array is ≈10 µm and the distance between adjacent patches is ≈10 µm. The gap distance between adjacent NTU units is around 30 µm. The center panel is a schematic of a perovskite/h-BN film.

layers as inorganic components, providing an excellent scaffold for exploring and tuning the carrier dynamic at the interfaces, which is supported by our time-resolved PL experiments and DFT calculations. Based on the novel optical behaviors, complex pattern-designed perovskite/h-BN vdW solids based light emission arrays are further fabricated. This work will shed light on organic perovskite based optoelectronic devices.

Experimental Section

Synthesis of Lead Halide Platelets: PbI_2 powder (99.999%, Aldrich) was used as a single source and put into a quartz tube mounted on a single-zone furnace (Lindberg/Blue MTF55035C-1). The freshly CVD graphene or MoS_2 or BN substrate (1 cm × 3 cm) was placed in the downstream region inside the quartz tube. The quartz tube was first evacuated to a base pressure of 3 mTorr, followed by a 50 sccm flow of high-purity Ar gas. The temperature and pressure inside the quartz tube were set and stabilized to desired values for each halide (390 °C and 30 Torr). In all cases, the synthesis was carried out within 30 min and the furnace was allowed to cool down naturally to ambient temperature.

Synthesis of CH_3NH_3I: The synthesis of CH_3NH_3I: 18.0 mL of methylamine (40 wt% in water, Sigma) was dissolved in 100 mL of absolute ethanol (absolute for analysis, Merck Millipore) in a 250 mL round bottom flask. 20.0 mL of hydroiodic acid (57 wt% in water, Alfa Aesar) was added into the solution dropwise. After that, the solution was stirred at 0 °C for 2 h. The raw product was obtained by removing the solvents using a rotary evaporator. A recrystallization process of the raw product, including the redissolution in 80 mL absolute ethanol and the precipitation after the addition of 300 mL diethyl ether, was carried out twice to get a much purer product. Finally, the white colored powders were collected and dried at 60 °C for 24 h in a vacuum oven.

Synthesis of Perovskites via the Reaction with CH_3NH_3I and PbI_2: The conversions were done using a similar CVD system. CH_3NH_3I were

used as a source and placed in the center of the quartz tube while CVD graphene or MoS_2 or BN substrate having as-grown lead halide platelets were placed around 5–6 cm away from the center in the downstream region. The quartz tube was first evacuated to a base pressure of 3 mTorr, followed by a 50 sccm flow of high-purity Ar gas. The pressure was then stabilized to 30 Torr and the temperature was elevated to 120 °C and kept there for 1 h after which the furnace was allowed to cool down naturally to ambient temperature.

Measurement: X-ray diffraction pattern (2θ scans) were obtained from perovskite/2D vdW solids supported on the SiO_2/Si substrates using an X-ray diffractometer (XRD Shimadzu Thin Film), using Cu Kα radiation (λ = 1.54050 Å) within a diffraction angle (2θ) from 5° to 60°. The SEM images of perovskite flakes were obtained using JEOL JEM7600F operated at an accelerating voltage of 10 kV. AFM experiments were performed in tapping mode under ambient conditions (Dimension ICON SPM system, Bruker, USA). Commercial silicon tips with a nominal spring constant of 40 N m^{-1} and resonant frequency of 300 kHz were used in all the experiments. The PbI_2 samples for transmission electron microscope (TEM) were flaked off from the 2D substrates by using toluene (99.85%, Acros Organics) and then transferred onto the TEM grids (Quantifoil Mo grids). The $CH_3NH_3PbI_3$ perovskite samples for TEM measurement were converted from the PbI_2 onto the TEM grids, with the similar method we introduced in the materials synthesis part above. The high resolution transmission electron microscopy (HRTEM) and the selected area electron diffraction (SAED) pattern were done with a FEI Tecnai F20 operated with an acceleration voltage of 200 kV. The chemical composition of lead iodide and $CH_3NH_3PbI_3$ perovskite was determined by means of energy dispersive X-ray spectroscopy (EDX attached to FEI TecnaiF20). A WITec alpha300 RAS Raman system with a piezocrystal controlled scanning stage, an objective lens of 100× magnification (numerical aperture, NA = 0.95), and an Electron Multiplying CCD was used for recording photoluminescence (PL) and Raman spectra/images. For PL spectra/images, a 600 lines mm^{-1} grating was used. For Raman spectra/images, a low-wavenumber coupler and a 2400 lines mm^{-1} grating were used for observing low-frequency Raman modes and achieving a good spectral resolution. All the PL

and Raman spectra/images were recorded under an excitation laser of 532 nm (E_{laser} = 2.33 eV). To avoid the laser-induced heating, laser power was kept below 0.1 mW. The laser spot was of ≈500 nm in diameter. UV–vis absorption spectra of perovskite/2D vdW solids prepared on quartz were recorded on SHIMADZU UV-3101PC UV–vis–NIR scanning spectrophotometer. The excitation pulse (400 nm) was generated by frequency doubling the 800 nm output (with a BBO crystal) from the Coherent Oscillator Mira 900F (120 fs, 76 MHz, 800 nm). The pump laser source was introduced into a microscope (Nikon LV100) and focused onto samples via a 20× objective (Nikon, numerical aperture: 0.4). The PL emission signal was collected in a standard backscattering geometry and dispersed by a 0.25 m DK240 spectrometer with 150 g mm^{-1} grating. The emission signal was time-resolved using an Optoscope Streak Camera system that has an ultimate temporal resolution of ≈10 ps. The fluorescence images were obtained by an Olympus fluorescence microscope. A mercury lamp was used as the excitation light source. All FL images are as taken without any artificial image processing.

h-BN Patterns Fabrication: As-transferred h-BN film could be used to prepare various patterns for inducing the growth of PdI$_2$ patterns. The fabrication process consisted of the following steps: (1) The h-BN film was covered by a photoresist layer spin-coated (AZ5214, 4000 rpm) on top of the h-BN surface; (2) Standard photolithography was performed to pattern the photoresist layer as a mask; (3) Argon-based plasma etching (power is 50 W, pressure is 200 mTorr and time is 30 s) was performed to transfer the photoresist mask pattern onto underlying h-BN; and (4) Photoresist mask was completely removed in acetone, and a h-BN pattern was created, such as the hexagon and "NTU" patterns shown in Figure S21 in the Supporting Information.

DFT Calculations: The results are based on first principle calculations within density functional theory (DFT) as implemented in the VASP[47] (Vienna ab initio simulation package) code. The ion–electron interaction was modeled by projector augmented plane wave (PAW)[48] and the electron exchange correlation was treated by Perdew–Burke–Ernzerhof (PBE) parameterization of the generalized gradient approximation (GGA).[49] The plane wave basis set with kinetic energy cutoff of 500 eV was used. The Brillouin zone was sampled by an $8 \times 8 \times 1$ Γ-centered k-point mesh. A vacuum layer of 15 Å was adopted to avoid interactions between the neighbor surfaces. All structures were fully relaxed until the Hellmann–Feynman force on each atom was smaller than 0.01 eV Å^{-1}.

Potential Energy Calculations: The energies were calculated by first-principles calculations as implemented in VASP code as well. Ultrasoft pseudopotentials were employed for the core region and spin-unpolarized density functional theory based on local density approximation, which could give a reasonable interlayer distance between the PbI$_2$ flake and *h*-BN sheet. A kinetic energy cutoff of 400 eV was chosen for the plane-wave expansion.

Supporting Information

Supporting Information is available from the Wiley Online Library or from the author.

Acknowledgements

[1] L. Britnell, R. V. Gorbachev, R. Jalil, B. D. Belle, F. Schedin, A. Mishchenko, T. Georgiou, M. I. Katsnelson, L. Eaves, S. V. Morozov, N. M. R. Peres, J. Leist, A. K. Geim, K. S. Novoselov, L. A. Ponomarenko, *Science* **2012**, *335*, 947.

[2] G. H. Lee, Y. J. Yu, X. Cui, N. Petrone, C. H. Lee, M. S. Choi, D. Y. Lee, C. Lee, W. J. Yoo, K. Watanabe, T. Taniguchi, C. Nuckolls, P. Kim, J. Hone, *ACS Nano* **2013**, *7*, 7931.

[3] N. J. Huo, J. Kang, Z. M. Wei, S. S. Li, J. B. Li, S. H. Wei, *Adv. Funct. Mater.* **2014**, *24*, 7025.

[4] L. Wang, I. Meric, P. Y. Huang, Q. Gao, Y. Gao, H. Tran, T. Taniguchi, K. Watanabe, L. M. Campos, D. A. Muller, J. Guo, P. Kim, J. Hone, K. L. Shepard, C. R. Dean, *Science* **2013**, *342*, 614.

[5] Y. J. Gong, J. H. Lin, X. L. Wang, G. Shi, S. D. Lei, Z. Lin, X. L. Zou, G. L. Ye, R. Vajtai, B. I. Yakobson, H. Terrones, M. Terrones, B. K. Tay, J. Lou, S. T. Pantelides, Z. Liu, W. Zhou, P. M. Ajayan, *Nat. Mater.* **2014**, *13*, 1135.

[6] G. L. Cui, M. Z. Zhang, G. T. Zou, *Sci. Rep.* **2013**, *3*, 1250.

[7] P. T. K. Loan, W. J. Zhang, C. T. Lin, K. H. Wei, L. J. Li, C. H. Chen, *Adv. Mater.* **2014**, *26*, 4838.

[8] I. Jahangir, A. Wilson, A. Singh, N. Sbrockey, E. Coleman, G. Tompa, G. Koley, presented at 14th IEEE Int. Conf. Nanotechnol., IEEE-NANO 2014, Toronto, Canada, August **2014**, p. 1000.

[9] G. Konstantatos, E. H. Sargent, *Nat. Nanotechnol.* **2010**, *5*, 391.

[10] L. Britnell, R. M. Ribeiro, A. Eckmann, R. Jalil, B. D. Belle, A. Mishchenko, Y. J. Kim, R. V. Gorbachev, T. Georgiou, S. V. Morozov, A. N. Grigorenko, A. K. Geim, C. Casiraghi, A. H. Castro Neto, K. S. Novoselov, *Science* **2013**, *340*, 1311.

[11] W. J. Zhang, C. P. Chuu, J. K. Huang, C. H. Chen, M. L. Tsai, Y. H. Chang, C. T. Liang, Y. Z. Chen, Y. L. Chueh, J. H. He, M. Y. Chou, L. J. Li, *Sci. Rep.* **2014**, *4*, 3826.

[12] M. Buscema, D. J. Groenendijk, S. I. Blanter, G. A. Steele, H. S. J. van der Zant, A. Castellanos-Gomez, *Nano Lett.* **2014**, *14*, 3347.

[13] O. Lopez-Sanchez, D. Lembke, M. Kayci, A. Radenovic, A. Kis, *Nat. Nanotechnol.* **2013**, *8*, 497.

[14] H. Wang, L. L. Yu, Y. H. Lee, Y. M. Shi, A. Hsu, M. L. Chin, L. J. Li, M. Dubey, J. Kong, T. Palacios, *Nano Lett.* **2012**, *12*, 4674.

[15] X. D. Xu, W. Yao, D. Xiao, T. F. Heinz, *Nat. Phys.* **2014**, *10*, 343.

[16] I. Zutic, J. Fabian, S. Das Sarma, *Rev. Mod. Phys.* **2004**, *76*, 323.

[17] T. Cao, G. Wang, W. P. Han, H. Q. Ye, C. R. Zhu, J. R. Shi, Q. Niu, P. H. Tan, E. Wang, B. L. Liu, J. Feng, *Nat. Commun.* **2012**, *3*, 887.

[18] J. Q. He, N. Kumar, M. Z. Bellus, H. Y. Chiu, D. W. He, Y. S. Wang, H. Zhao, *Nat. Commun.* **2014**, *5*, 5622.

[19] C. R. Dean, A. F. Young, I. Meric, C. Lee, L. Wang, S. Sorgenfrei, K. Watanabe, T. Taniguchi, P. Kim, K. L. Shepard, J. Hone, *Nat. Nanotechnol.* **2010**, *5*, 722.

[20] A. Ramasubramaniam, D. Naveh, E. Towe, *Nano Lett.* **2011**, *11*, 1070.

[21] R. Cheng, D. H. Li, H. L. Zhou, C. Wang, A. X. Yin, S. Jiang, Y. Liu, Y. Chen, Y. Huang, X. F. Duan, *Nano Lett.* **2014**, *14*, 5590.

[22] N. Lu, H. Y. Guo, L. Li, J. Dai, L. Wang, W. N. Mei, X. J. Wu, X. C. Zeng, *Nanoscale* **2014**, *6*, 2879.

[23] S. D. Stranks, G. E. Eperon, G. Grancini, C. Menelaou, M. J. Alcocer, T. Leijtens, L. M. Herz, A. Petrozza, H. J. Snaith, *Science* **2013**, *342*, 341.

[24] H. S. Kim, I. Mora-Sero, V. Gonzalez-Pedro, F. Fabregat-Santiago, E. J. Juarez-Perez, N. G. Park, J. Bisquert, *Nat. Commun.* **2013**, *4*, 2242.

[25] N. J. Jeon, J. H. Noh, Y. C. Kim, W. S. Yang, S. Ryu, S. I. Seok, *Nat. Mater.* **2014**, *13*, 897.

[26] P. Docampo, J. M. Ball, M. Darwich, G. E. Eperon, H. J. Snaith, *Nat. Commun.* **2013**, *4*.

[27] K. Tanaka, T. Takahashi, T. Ban, T. Kondo, K. Uchida, N. Miura, *Solid State Commun.* **2003**, *127*, 619.

[28] K. Liang, D. B. Mitzi, M. T. Prikas, *Chem. Mater.* **1998**, *10*, 403.

[29] G. Xing, N. Mathews, S. S. Lim, N. Yantara, X. Liu, D. Sabba, M. Grätzel, S. Mhaisalkar, T. C. Sum, *Nat. Mater.* **2014**, *13*, 476.

[30] N. G. Park, *J. Phys. Chem. Lett.* **2013**, *4*, 2423.

[31] A. K. Geim, I. V. Grigorieva, *Nature* **2013**, *499*, 419.

[32] S. J. Haigh, A. Gholinia, R. Jalil, S. Romani, L. Britnell, D. C. Elias, K. S. Novoselov, L. A. Ponomarenko, A. K. Geim, R. Gorbachev, *Nat. Mater.* **2012**, *11*, 764.

[33] K. Kosmider, J. Fernandez-Rossier, *Phys. Rev. B* **2013**, *87*, 075451.

[34] Y. Sakai, S. Saito, *J. Phys. Soc. JPN.* **2012**, *81*, 103701.

[35] Z. Liu, L. Song, S. Zhao, J. Huang, L. Ma, J. Zhang, J. Lou, P. M. Ajayan, *Nano Lett.* **2011**, *11*, 2032.

[36] W. Yang, G. Chen, Z. Shi, C. C. Liu, L. Zhang, G. Xie, M. Cheng, D. Wang, R. Yang, D. Shi, K. Watanabe, T. Taniguchi, Y. Yao, Y. Zhang, G. Zhang, *Nat. Mater.* **2013**, *12*, 792.

[37] M. Wang, S. K. Jang, W. J. Jang, M. Kim, S. Y. Park, S. W. Kim, S. J. Kahng, J. Y. Choi, R. S. Ruoff, Y. J. Song, S. Lee, *Adv. Mater.* **2013**, *25*, 2746.

[38] X. D. Duan, C. Wang, J. C. Shaw, R. Cheng, Y. Chen, H. L. Li, X. P. Wu, Y. Tang, Q. L. Zhang, A. L. Pan, J. H. Jiang, R. Q. Yu, Y. Huang, X. F. Duan, *Nat. Nanotechnol.* **2014**, *9*, 1024.

[39] C. M. Huang, S. F. Wu, A. M. Sanchez, J. J. P. Peters, R. Beanland, J. S. Ross, P. Rivera, W. Yao, D. H. Cobden, X. D. Xu, *Nat. Mater.* **2014**, *13*, 1096.

[40] T. Baikie, Y. Fang, J. M. Kadro, M. Schreyer, F. Wei, S. G. Mhaisalkar, M. Graetzel, T. J. White, *J. Mater. Chem. A* **2013**, *1*, 5628.

[41] R. Zallen, M. L. Slade, *Solid State Commun.* **1975**, *17*, 1561.

[42] M. Khilji, W. Sherman, G. Wilkinson, *J. Raman Spectrosc.* **1982**, *13*, 127.

[43] S. T. Ha, X. Liu, Q. Zhang, D. Giovanni, T. C. Sum, Q. Xiong, *Adv. Opt. Mater.* **2014**, *2*, 838.

[44] V. D'Innocenzo, G. Grancini, M. J. P. Alcocer, A. R. S. Kandada, S. D. Stranks, M. M. Lee, G. Lanzani, H. J. Snaith, A. Petrozza, *Nat. Commun.* **2014**, *5*, 3586.

[45] Z. L. Zhu, J. A. Ma, Z. L. Wang, C. Mu, Z. T. Fan, L. L. Du, Y. Bai, L. Z. Fan, H. Yan, D. L. Phillips, S. H. Yang, *J. Am. Chem. Soc.* **2014**, *136*, 3760.

[46] Y. Lee, J. Kwon, E. Hwang, C. H. Ra, W. J. Yoo, J. H. Ahn, J. H. Park, J. H. Cho, *Adv. Mater.* **2015**, *27*, 41.

[47] G. Kresse, J. Hafner, *Phys. Rev. B* **1994**, *49*, 14251.

[48] P. E. Blochl, *Phys. Rev. B* **1994**, *50*, 17953.

[49] J. P. Perdew, K. Burke, M. Ernzerhof, *Phys. Rev. Lett.* **1996**, *77*, 3865.